

# Detecting Mitoses in Time-Lapse Images of Embryonic Epithelia Using Intensity Analysis

PARTHIPAN SIVA,<sup>1</sup> G. WAYNE BRODLAND,<sup>2,3</sup> and DAVID CLAUSI<sup>1</sup>

<sup>1</sup>Department of Systems Design Engineering, University of Waterloo, Waterloo, ON N2L 3G1, Canada; <sup>2</sup>Department of Civil and Environmental Engineering, University of Waterloo, Waterloo, ON N2L 3G1, Canada; and <sup>3</sup>Department of Biology, University of Waterloo, Waterloo, ON N2L 3G1, Canada

(Received 3 July 2009; accepted 31 August 2009)

**Abstract**—Although the frequency and orientation of mitoses can significantly affect the mechanics of early embryo development, these data have not been available due to a shortage of suitable automated techniques. Fluorescence imaging, though popular, requires biochemical intervention and is not always possible or desirable. Here, a new technique that takes advantage of a localized intensity change that occurs in bright field images is used to identify mitoses. The algorithm involves mapping a deformable, sub-cellular triangular mesh from one time-lapse image to the next so that corresponding regions can be identified. Triangles in the mesh that undergo darkening of a sufficient degree over a period consistent with mitosis are flagged. Mitoses are assumed to occur along the short axis of elliptical areas fit to suitably sized clusters of flagged triangles. The algorithm is less complex than previous approaches and it has strong discrimination characteristics. When applied to 15 image sets from neurulation-stage axolotl (*Ambystoma mexicanum*) embryos, it was able to correctly detect 86% of the manually identified mitoses, had less than 5% false positives and produced average angular errors of only 15°. The new algorithm is simpler to implement than those previously available, is substantially more accurate, and provides data that is important for understanding the mechanics of morphogenetic movements.

**Keywords**—Mitosis identification, Mitosis orientation, Embryonic epithelia, Morphogenetic movements, Axolotl.

## INTRODUCTION

During early embryo development, sheets of cells called epithelia undergo significant self-driven changes of shape (Fig. 1) in order to form organs and other essential structures. Experiments and computational models have shown that mitosis can significantly affect

the mechanics of these cell sheets, especially if the mitoses have non-random orientations within the sheet.<sup>7,10</sup> Although, in principal, mitoses can be identified manually by the characteristic local motion patterns and reflectance changes they produce in bright field images (Fig. 2), such work is tedious and makes detailed studies impractical.

A number of attempts have been made to solve this problem. Cells grown in culture are often separated spatially from each other, and if the right combinations of imaging methodologies and segmentation algorithms are used, mitoses can be identified by changes in topology.<sup>2,3,5,27</sup> If cells are confluent but have sufficient edge contrast, the segmentation step can be done using boundary algorithms.<sup>17,23,25,33,38</sup> Edge contrast can often be enhanced using fluorescent membrane markers, but biochemical interventions are involved and they may affect the behavior of the cells. Because cells in axolotl embryos are contiguous, have unreliable edge contrast, and fluorescent markers are not currently available for early stage embryos of this species, none of these approaches is suitable. A previous algorithm developed by the authors Siva *et al.*<sup>30</sup> used image processing and pattern recognition methods to identify localized deformation patterns characteristic of mitosis, thereby avoiding the segmentation problem. That approach was able to achieve identification accuracies slightly less than 70% and average orientation errors of 27°.

In order to improve on these values, a new algorithm that detects transient changes in surface reflectance was developed and, like its predecessor, it circumvents the need to find all of the cell boundaries. The optical characteristics of these cells derive from the presence and motion of pigment granules on the cell surface.<sup>11</sup> In the early-stage embryonic epithelia of interest here, a dark band arises along the junction between the newly formed daughter cells (Fig. 2), a phenomenon observed in a variety of other kinds of tissues, including those

---

Address correspondence to G. Wayne Brodland, Department of Civil and Environmental Engineering, University of Waterloo, Waterloo, ON N2L 3G1, Canada. Electronic mail: psiva@uwaterloo.ca, brodland@uwaterloo.ca, dclausi@uwaterloo.ca. URL: www.psiva.ca, www.civil.uwaterloo.ca/brodland, www.eng.uwaterloo.ca/dclausi/

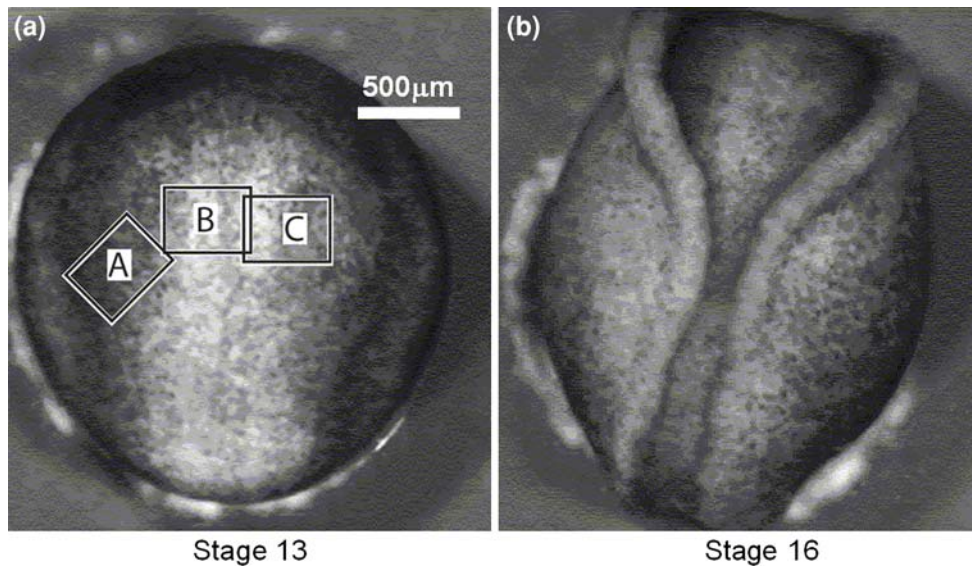


**FIGURE 1.** Dorsal view of a neurulation-stage axolotl embryo. The cephalic end of the embryo is toward the top of the image and the caudal end toward the bottom. (a) Stage 13; (b) Stage 16.

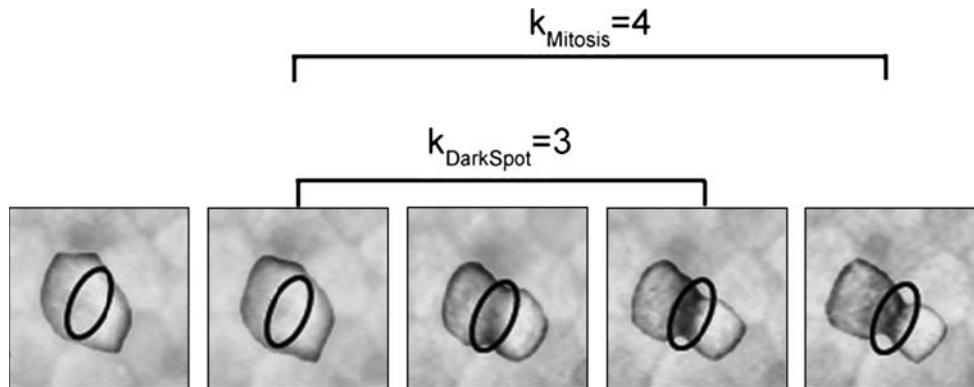


**FIGURE 2.** Close-up of a single mitosis. The intensity drop outlined by the ellipse occurs as the cell undergoes mitosis. The time in frames for mitosis and the appearance of the dark spot are indicated.

associated with breast cancer.<sup>19</sup> A previous study by the authors suggested that mitoses in very early-stage embryos could be identified by these dark bands,<sup>31</sup> which evidently arise from the localization of pigment. The present study generalizes that finding to later-stage tissues and provides a means to determine mitosis orientation. In brief, the algorithm places a regular, sub-cellular mesh on one frame of the image sequence and uses tracking methods to map it to subsequent images so that each triangle continues to overlay the same portion of the same cell. Triangles in which sufficient reductions in intensity occur over a period consistent with mitoses are then identified and elliptical areas are fit to suitable clusters of such triangles. Mitoses are assumed to occur at the centroids of these ellipses and to be oriented along their short axes. When suitable algorithms for each of these steps were found and linked appropriately, the resulting method was simpler

than previous ones and substantially more accurate. The new mitosis data it provides—spatial distributions, frequencies and orientations—are an important addition to the motion,<sup>8,18</sup> strain,<sup>37</sup> stress,<sup>1</sup> and fabric<sup>17</sup> data currently available to those investigating the mechanics of morphogenetic movements.

## REGION REGISTRATION

The first major step in the algorithm is to associate corresponding regions in one time-lapse image with those in the next. Since the morphogenetic movements of interest here can cause tissues to move substantially (Fig. 1), large bulk translations can occur from one image to the next. These bulk translations are removed using normalized cross-correlation on the entire image.<sup>30</sup>

This approach works well because the intensity changes produced by mitoses are highly localized and affect only a small fraction of the total image area. Previous studies<sup>30,36</sup> have shown that the remaining deformation fields are smooth under normal circumstances, considerably simplifying the mapping problem, and allowing a variety of options to be considered. Here, a regular mesh (material reference frame)<sup>24,26,34</sup> consisting of subcellular-sized triangles is used to map corresponding areas of the image to each other. Meshes are matched from frame-to-frame using identifiable triple junctions (TJs), because these points are well defined and, although irregularly spaced, are sufficiently dense (Fig. 3a) that regions can be matched reliably. Also, unlike points inside the cells, they are not affected by mitosis-induced intensity changes.

Accurate identification of triple points involves a series of steps, starting with the application of Gabor filters (GF) tuned to the pixel width of the cell boundaries<sup>33</sup> and applied at  $0$ ,  $\pm 45^\circ$ , and  $90^\circ$ . The four resulting filtered images are then composited (Fig. 3b) by selecting the maximum of the second norm at each pixel. Too thin the lines produced by this process, phase thresholding<sup>29</sup> and skeletonization<sup>14</sup> are applied giving a binary image in which cell boundaries are no more than one pixel wide (Fig. 3c). Due to low image contrast and high noise in the images, this approach does not yield complete cell boundaries—the main reason that mitoses cannot be identified directly from these images—and it produces some short false boundaries.

A variety of options exist for identifying TJs in these binary images.<sup>20,22,32</sup> The quality of the binary images is sufficient that candidate triple junctions can be found by identifying 3 by 3 pixel neighborhoods homologous with the three shown in Fig. 4 and their rotated forms (mirrored forms would be redundant). This set of 12 prototypes covers all possible skeletonized triple junctions. To eliminate false triple junctions produced by very short branches arising from

edge-adjacent noise, a circle of radius  $R$  was traced around each candidate TJ. The circle radius was set to three times the average cell boundary width (in the neurulation image sets, for example, this was typically 10 pixels or  $7 \mu\text{m}$ ). If at least three branches from a candidate TJ crossed the circle, the candidate TJ was considered a true triple junction or key point, as identified by the circles in Fig. 3c.

When mitosis rates are high, as they are during gastrulation, local displacements occur causing the templates to be matched to locations that are randomly displaced about the true locations. The random displacements

$$Q_k \sim N(0, q) \quad (1)$$

of a particular point in frame number  $k$  of the image sequence are assumed to be Gaussian with zero mean and covariance  $q$ . To ameliorate the effects of this “noise” a Kalman Filter (KF)<sup>35</sup> is used to track points in frame  $F_k$  to frame  $F_{k+1}$ .<sup>29</sup> The filter improves on the tracked position of any particular point in  $F_{k+1}$ , by using a dynamic model that describes how that point is expected to move and by providing information about its current velocity (based on the difference in its tracked positions between  $F_k$  and  $F_{k+1}$ ) to the model. The KF has three steps, the first of which is to calculate the new position  $(x, y)$  of the point based on the dynamic model. Here, the simplest model is assumed;

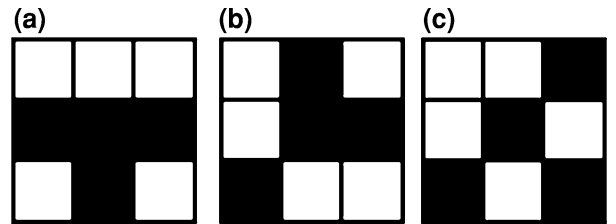


FIGURE 4. Masks used to identify triple junction points.

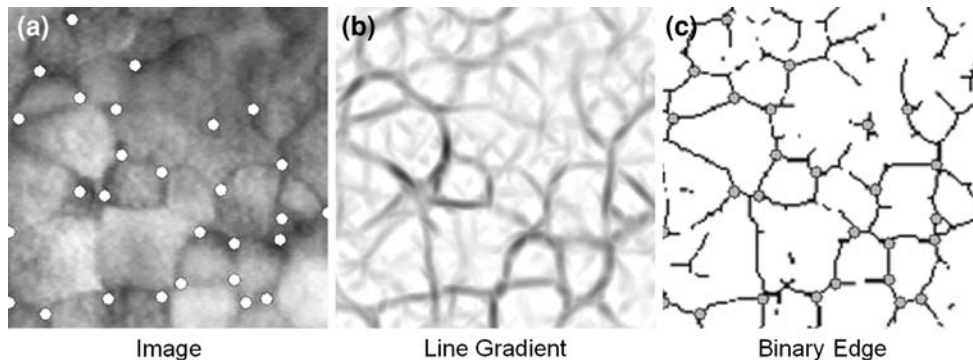


FIGURE 3. Extraction of cell boundaries and junction points. (a) Original image; (b) Line gradient; (c) One pixel thick cell boundary. The detected junction points are marked by circles in (a) and (c).

namely that the velocity of each point is equal to its average velocity up to that frame. The KF defines a state vector

$$\mathbf{z}_{k+1} = [x, y, v_x, v_y]^T \quad (2)$$

for each tracked point associated with  $F_{k+1}$  where the first two components of  $\mathbf{z}_{k+1}$  give the location of the point in  $F_{k+1}$  and the last two components its velocity between  $F_k$  and  $F_{k+1}$ . The dynamic model is then written in the form

$$\mathbf{z}_{k+1} = \mathbf{A}\mathbf{z}_k + \mathbf{w}_k \quad (3)$$

where

$$\mathbf{A} = \begin{bmatrix} 1 & 0 & \Delta t & 0 \\ 0 & 1 & 0 & \Delta t \\ 0 & 0 & 1 & 0 \\ 0 & 0 & 0 & 1 \end{bmatrix} \quad (4)$$

where each component of the vector  $\mathbf{w}_k$  is a Gaussian distribution

$$\mathbf{w}_k \sim N(0, R), \quad (5)$$

with a variance of  $R = 4$  pixels, a value found to be suitable for all of the image sets, and  $\Delta t$  is the time difference between frames  $F_k$  and  $F_{k+1}$ .

The next step in the KF is to track each of the key points from  $F_k$  to  $F_{k+1}$ , and here this is done using normalized cross-correlation template matching.<sup>36</sup> A template of size  $n$  by  $n$  centered on each key point is searched within an  $N$  by  $N$  search area around its predicted location  $(x, y)$  in  $F_{k+1}$  as given by Eqs. (3) and (4). The location of the maximum correlation value is taken as the key point location  $\mathbf{m}_{k+1} = [x^*, y^*]^T$ . In order to characterize the uncertainty in  $\mathbf{m}_{k+1}$ , the 2 by 2 covariance matrix  $\mathbf{Q}_t$  of the  $N$  by  $N$  cross-correlation matrix is calculated.<sup>28</sup> To maintain invariance with respect to image resolution, the template size  $n$  is chosen to be approximately three times the cell boundary width in pixels and the search area  $N$  is chosen to be of the order of the average cell size in pixels. Average cell size can be obtained manually or using an automated algorithm such as Iles *et al.*<sup>17</sup> In the gastrulation images,  $n = 10$  and  $N = 22$ , while for the neurulation images  $n = 15$  and  $N = 76$ .

The final step in the KF estimates the actual point location  $\mathbf{g}_{k+1}$  based on the model prediction  $\mathbf{z}_{k+1}$ , its uncertainty  $\mathbf{w}_k$ , the measured point position  $\mathbf{m}_{k+1}$  and its uncertainty  $\mathbf{Q}_t$ . This is done on a point-by-point basis frame-by-frame using the equations<sup>35</sup>

$$\mathbf{P}_0 = 100\mathbf{I} \quad (6)$$

$$\mathbf{K}_{k+1} = \mathbf{P}_k \mathbf{C}^T (\mathbf{C} \mathbf{P}_k \mathbf{C}^T + \mathbf{Q}_{k+1})^{-1} \quad (7)$$

$$\mathbf{P}_{k+1} = \mathbf{P}_k - \mathbf{K}_{k+1} \mathbf{C} \mathbf{P}_k \quad (8)$$

$$\mathbf{g}_{k+1} = \mathbf{z}_{k+1} + \mathbf{K}_{k+1} (\mathbf{m}_{k+1} - \mathbf{C} \mathbf{z}_{k+1}) \quad (9)$$

where

$$\mathbf{C} = \begin{bmatrix} 1 & 0 & 0 & 0 \\ 0 & 1 & 0 & 0 \end{bmatrix} \quad (10)$$

The KF steps, which end here, provide an estimated location  $\mathbf{g}_{k+1}$  for each of the key points.

During tracking it is possible for key points to drift away from their actual TJ<sup>36</sup> or to be untrackable due to low image contrast. To manage this situation, if a key point at estimated location  $\mathbf{g}_{k+1}$  is not within  $d$  pixels of a TJ in frame  $F_{k+1}$ , it assumed to be lost, and a new TJ is added to the list of key points in  $F_{k+1}$ . The newly added TJ must be at least  $d$  pixels away from any existing TJs and not closer than 3 cell diameters from the image border so that it does not displace out of the field of view.

Next, these key points are used to determine how a uniform triangular mesh defined by a set of vertices  $\mathbf{S}_0 = \{\underline{h}_1, \dots, \underline{h}_L\}$  in the first image map successively from frame  $F_k$  to frame  $F_{k+1}$ . Mesh vertices are mapped from  $\mathbf{S}_k$  to  $\mathbf{S}_{k+1}$  using an algorithm developed by Pilet *et al.*<sup>24</sup> In brief this algorithm obtains  $\mathbf{S}_{k+1}$  by minimizing the objective function

$$\mathbf{S}_{k+1} = \arg \min_{\mathbf{S}_{k+1}} \varepsilon(\mathbf{S}_{k+1}) \quad (11)$$

$$\varepsilon(\mathbf{S}_{k+1}) = \varepsilon_d(\mathbf{S}_{k+1}) + \varepsilon_c(\mathbf{S}_k, \mathbf{S}_{k+1}, F_k, F_{k+1}),$$

which involves two constrains:  $\varepsilon_c$ , which ensures that key points are followed; and  $\varepsilon_d$ , which causes otherwise unconstrained points in the mesh to deform like a rubber sheet.<sup>36</sup>

An efficient deformation constraint  $\varepsilon_d$  can be constructed using a banded matrix  $\mathbf{L}$ , details of which are given in Siva,<sup>29</sup> which is associated with the second derivative of displacements of adjacent vertices and vectors  $\mathbf{X}$ ,  $\mathbf{Y}$  composed, respectively, of all of the  $x$  and  $y$  coordinates of the mesh vertices listed in  $\mathbf{S}_{k+1}$ .<sup>16,24</sup>

The resulting function

$$\varepsilon_d(\mathbf{S}_{k+1}) = 0.5(\mathbf{X}^T \mathbf{L} \mathbf{X} + \mathbf{Y}^T \mathbf{L} \mathbf{Y}) \quad (12)$$

can be considered a type of strain energy measure.

Here, the constraint  $\varepsilon_c$  is formulated as<sup>24</sup>

$$\begin{aligned} \varepsilon_c(\mathbf{S}_k, \mathbf{S}_{k+1}, F_k, F_{k+1}) \\ = -\sum_i \rho(\|F_{k+1}(i) - T_s(F_k(i), \mathbf{S}_k, \mathbf{S}_{k+1})\|, r) \end{aligned} \quad (13)$$

where  $T_s(\cdot)$  is a function that maps a point in a single triangle in frame  $F_k$  to its new location in  $F_{k+1}$  based on the location  $\mathbf{S}_{k+1}$  of the mesh points defining that triangle in  $F_{k+1}$  and the barycentric triplet<sup>15</sup> describing the position of that point in its triangle.<sup>29</sup>

The function  $\rho(\delta, r)$  was chosen as

$$\rho(\delta, r) = 3(r^2 - \delta^2)/(4r^3) \quad (14)$$

where the value of  $r$ , as obtained from Pilet *et al.*,<sup>24</sup> starts as a large number and decreases after each iteration of the objective function (Eq. 11). The starting value for  $r$  was chosen as  $3\Delta_{\text{Max}}$  where  $\Delta_{\text{Max}}$  is the maximum possible displacement of a key point between frame  $k$  and  $k + 1$ .

By iteratively solving Eq. (11),<sup>24</sup> the triangular mesh can be deformed from one frame to the next over the entire image sequence. Since we seek patterns of intensity change that span distances smaller than a cell, the triangular mesh must have elements substantially smaller than a typical cell. In this study, we found that triangles with a side length not greater than 1/10 the diameter of a typical cell gave reliable results.

### INTENSITY ANALYSIS

Having established a means to map sub-cellular triangular regions from frame-to-frame throughout the time lapse image sequence, the next step is to identify those triangular regions in which the intensity decreases (i.e., the reflectance decreases) sufficiently over a period of time consistent with mitosis. The image intensity for each triangular region  $i$ , is defined as the average intensity of all image pixels within that triangle  $G_k(i)$ . Figures 5a–5d show selected time-lapse frames while Fig. 5e shows the corresponding triangles colored according to their average values. The greatest changes occur between a frame taken before mitosis begins and one taken at the middle of the process, and these frames may not be successive. Thus, the intensity change for triangular area  $i$  is defined as

$$U_k(i) = G_k(i) - \min(G_{k+1}(i), G_{k+2}(i), \dots, G_{k+k_{\text{Mitosis}}}(i)) \quad (15)$$

The value of  $k_{\text{Mitosis}}$  is chosen by the user such that it represents the largest number of frames that a typical mitosis spans. Negative values of  $U_k(i)$  are set to zero because only decreases in intensity, which produce the light-colored triangles in Fig. 5f, are of interest here.

Next, the triangles in  $U_k$  are qualified with respect to intensity, spatial distribution, and duration. Triangles with lighter initial intensities were found to change more during mitosis than did those which were initially darker. To utilize this observation, the intensity change qualification threshold for each triangle was made a function

$$U'_k(i) = \begin{cases} 1 & U_k(i) > G_k(i)T_m + T_b \\ 0 & \text{Otherwise} \end{cases} \quad (16)$$

of its intensity  $G_k(i)$ , where  $T_m$  and  $T_b$  are slope and  $y$ -intercept parameters, respectively, obtained by fitting

a line through a plot of  $G_k(i)$  vs.  $U_k(i)$  for 2–5 manually identified mitoses in the image set.<sup>29</sup>

At this point, most of the triangles in the mesh are set to zero, and the non-zero triangles correspond to actual mitosis, noise induced by tracking errors and shadows created by cell boundaries. To remove noise artefacts, a size threshold  $T_{\text{Size}}$  is applied to each set of contiguous triangles (a blob). The size is measured as the number of mesh triangles in the blob and any blobs smaller than the size threshold are set to zero. The size threshold  $T_{\text{Size}}$  is set to half the number of mesh triangles needed to span an average cell with a filled-in ribbon one triangle wide. For good blob discrimination, the resulting number of triangles should be at least 10.

The remaining collections of triangles (blobs) are then qualified in terms of their duration. Given  $k_{\text{Mitosis}}$ , the number of frames that a typical mitosis lasts and  $k_{\text{DarkSpot}}$  the characteristic number of frames until the appearance of the dark band produced by mitosis (Fig. 2), the expected duration of blobs can be estimated as  $k_{\text{Mitosis}} - k_{\text{DarkSpot}} + 1$  frames. A blob in frame  $t$  is said to be present in frame  $k + 1$  if there is a blob in frame  $k + 1$  that spatially overlaps the blob from frame  $k$ . Any blobs that do not have a duration of at least  $k_{\text{Mitosis}} - k_{\text{DarkSpot}} + 1$  frames are deleted. The result of this process is a series of blobs that span several consecutive frames (Fig. 5g). The union of these blobs, Fig. 5h, are assumed to represent a single mitosis. An elliptical area is fit to this union of triangular meshes over time using an Eigen-decomposition<sup>29</sup> of its area. The centroid of the ellipse is defined as the location of the mitosis and the direction of the minor-axis of the ellipse is assumed to correspond to the direction of the mitosis.

### RESULTS AND CONCLUSIONS

The intensity-based algorithm defined in the previous sections was used to investigate mitosis in 15 time-lapse image sets from early-stage embryos (Stages 9–10)<sup>4</sup> of the axolotl (*Ambystoma mexicanum*), a type of amphibian. The data are the same as those to which the earlier motion-based algorithm was applied.<sup>30</sup> The gastrulation-stage sequence consisted of 25 images collected at 5-min intervals from region A in Fig. 1 and the images had 400 pixels per mm. Fourteen sequences from late gastrulation and early neurulation (Stages 12–13), here identified as being “neurulation-stage”, were collected at 1-min intervals from regions B and C and there were 1400 pixels per mm. The lenses had sufficient numerical apertures that the resolution was not diffraction limited.

Ground truth was determined using a custom Matlab interface that made it possible to play single or

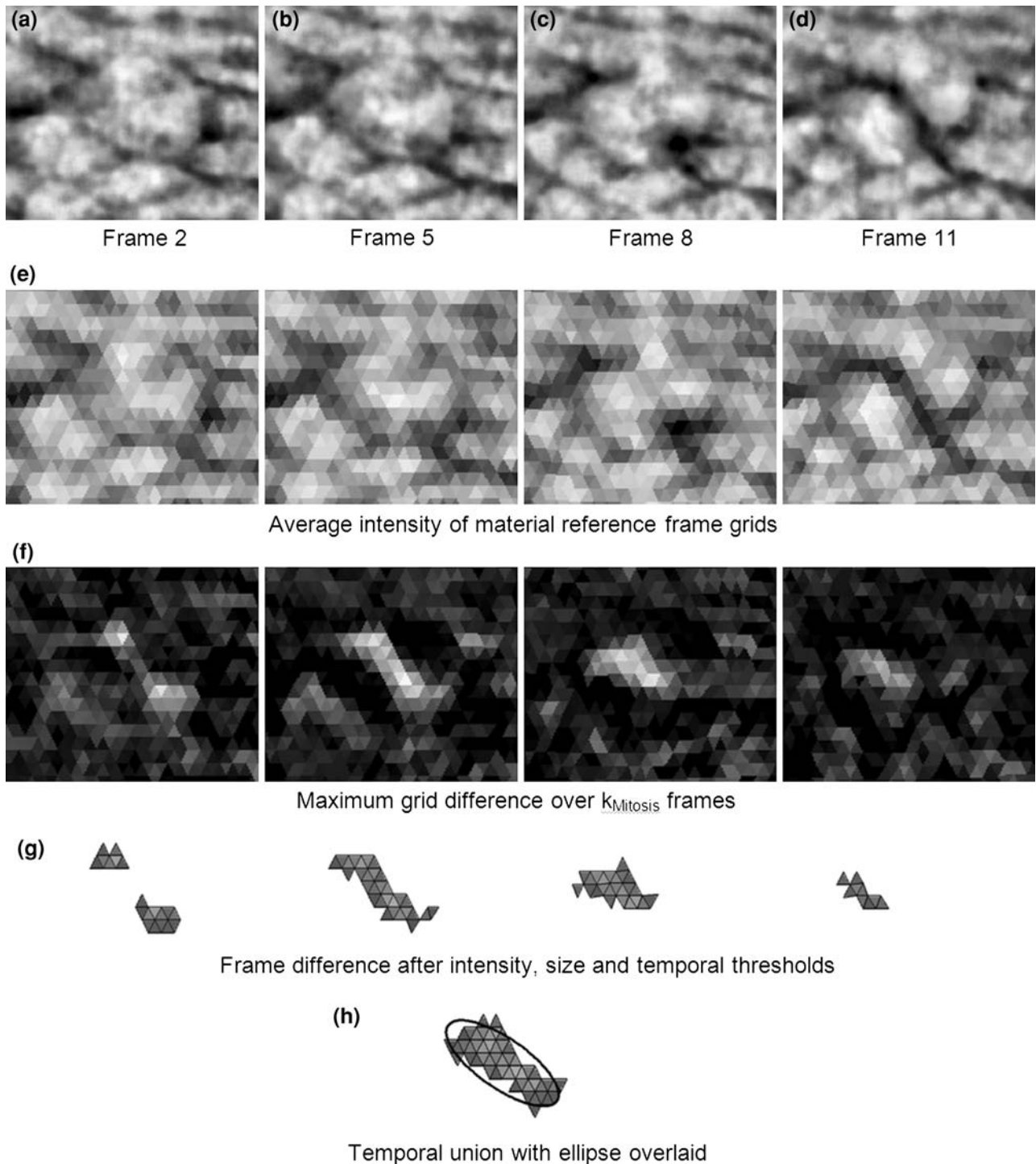


**FIGURE 5.** Overview of mitosis identification process. (a)–(d) Selected, cropped frames from a time-lapse image set showing a single mitosis; (e) Graphic representation of the average intensity of each triangle in the material reference frame; (f) Maximum frame difference  $U_t$  over  $k_{\text{Mitosis}}$  frames; (g) Triangles that remain following intensity, blob size, and duration thresholding; and (h) An ellipse fit to the union of the thresholded triangles. The short axis of the ellipse indicates the mitosis direction.

multiple frames forward or back so that mitoses could be identified manually. When any single cell became visible as two cells, a mitosis was deemed to have occurred and its location and orientation was deter-

mined by drawing a short line along the newly formed border using the Matlab tool. These ground truth data were used for evaluating the output of the automated intensity-based algorithm.

Precision of the algorithm, a measure of the fraction of the mitoses identified by the algorithm that actually are mitoses, is defined as

$$P = \frac{TP}{TP + FP} \quad (17)$$

where  $TP$  is the number of true positives and  $FP$  the number of false positives. Recall, also called the true positive rate, is the fraction of mitosis correctly detected by the algorithm out of the total mitosis present in the test data set, and is given by

$$R = \frac{TP}{TP + FN} \quad (18)$$

where  $FN$  is the number of false negatives. The performance of an algorithm relative to a parameter in that algorithm can be studied using the precision–recall curve (Fig. 6), a curve related to the receiver operator curve (ROC),<sup>13</sup> and commonly used to evaluate classification algorithms.

The performance rate or score for a given algorithm can be calculated using the  $F$ -measure<sup>21</sup>

$$F_\beta = \frac{(\beta^2 + 1)PR}{\beta^2 P + R}, \quad (19)$$

where the parameter  $\beta$  controls the importance of recall over precision. In this study both precision and recall are assumed to be equally important, and  $\beta$  is set to 1.

The parameters  $t_{\text{Mitosis}} - t_{\text{DarkSpot}} + 1$ ,  $T_m$ ,  $T_b$ ,  $T_{\text{Size}}$  used in the algorithm (Table 1) were selected using 3 of the 94 manually detected mitoses for the gastrulation-stage and using image sequences containing 1 mitosis each, for the neurulation-stage sets. In the gastrulation-stage series the algorithm correctly detected 65 of the 91 mitosis and made 20 false

detections. In neurulation-stage sets it correctly detected 18 of the 21 mitosis and made only 1 false detection. Mitoses used to determine the algorithm parameters were not included in these calculations. The algorithm performed significantly better on the neurulation-stage images than on the gastrulation-stage images because of the shorter interval between consecutive frames and the lower incidence of mitoses, which reduced the probability of immediately adjacent mitoses occurring simultaneously and their blobs overlapping with each other. In both the gastrulation and neurulation-stages the intensity-based algorithm, with scores of 74 and 90%, respectively, significantly outperformed the motion-based algorithm, which had scores of 68 and 67%.

In terms of mitosis orientation, the mean error for gastrulation-stage images was  $40^\circ$  with a standard deviation of  $29^\circ$ , and these rather large errors were a consequence of the low magnification of the images (18.5 pixels per cell, and 6 triangles per cell). The neurulation-stage image sets were of higher magnification (42.9 pixels per cell, and 12 triangles per cell) and the mitosis orientation error was much lower, with a mean error of  $15^\circ$  and a standard deviation of  $19^\circ$  (Fig. 7), as compared to the motion-based algorithm,

TABLE 1. Intensity algorithm parameters.

Image set	Qualification type			
	Intensity change		Blob size $T_{\text{Size}}$	Blob duration $k_{\text{Mitosis}} - k_{\text{DarkSpot}} + 1$
	$T_m$	$T_b$		
Gastrulation	0.275	0.020	5	2
Neurulation	0.039	0.294	5	5

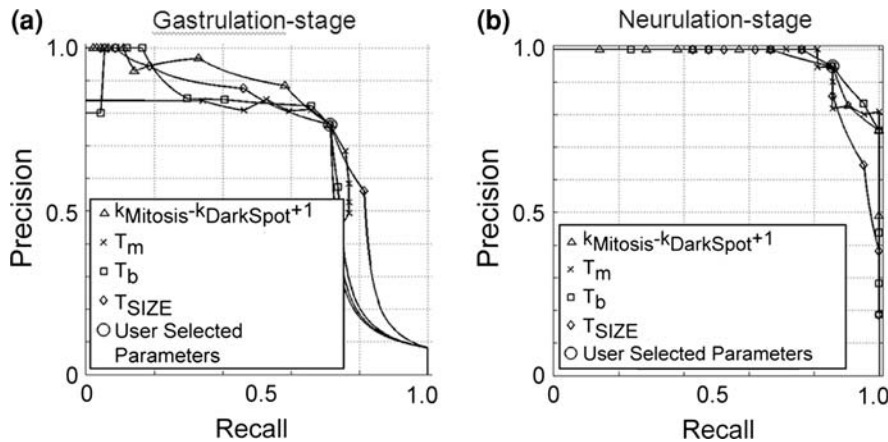
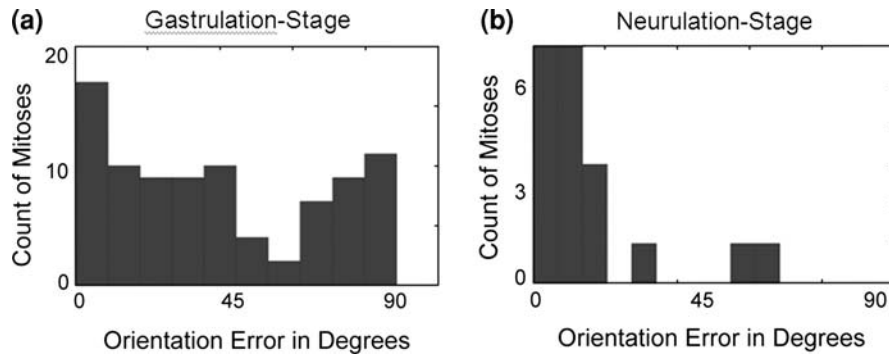
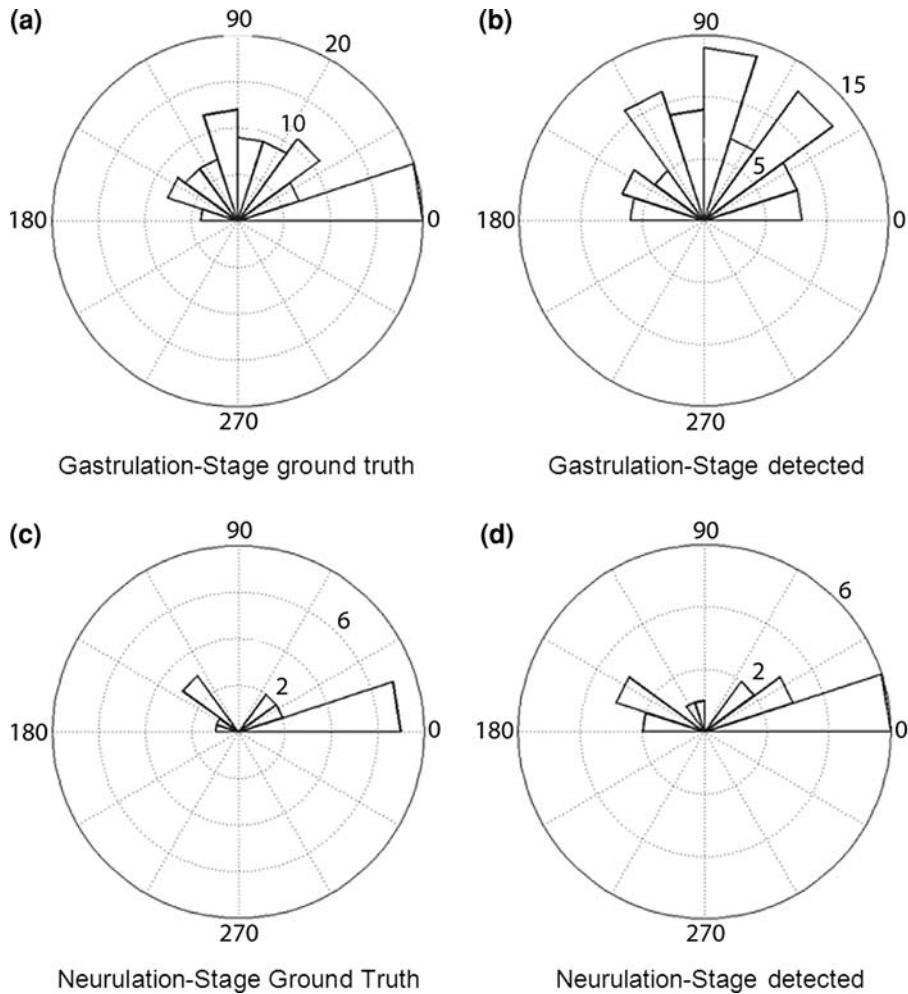


FIGURE 6. Precision–recall curves. Curves for (a) gastrulation- and (b) neurulation-stage image sets. The parameter  $Q$  in the graphs is equal to  $k_{\text{Mitosis}} - k_{\text{DarkSpot}} + 1$ .



**FIGURE 7.** Orientation error histograms. The histograms show the angular error between ground truth and algorithmically detected mitoses.



**FIGURE 8.** Ground truth and algorithmically detected mitosis orientation histograms.

which had a mean error of  $35^\circ$ .<sup>30</sup> More than 80% of the mitosis identified during neurulation were within  $15^\circ$  of their true orientations.

As we have noted previously,<sup>30</sup> that the lack of a clear angular preference for mitosis during gastrulation (Fig. 8) is consistent with the relatively isotropic fabric

of the cells at that stage and with the relatively modest strain rates associated with all but the region near the blastopore. The high rate of mitosis is consistent with the need for the epidermis to expand as tissue involutes through the blastopore. Interestingly, the cells do not grow in volume following division, but the geometry of



the daughter cells and the force imbalance it creates predisposes the cell sheet to in-plane expansion.<sup>12</sup>

During neurulation, significant convergent extension (narrowing in the medio-lateral direction and elongation in the cephalo-caudal direction) begins to occur in the regions where the images were captured. Individual cells become elongated in the medio-lateral direction to the extent that their average aspect ratio reaches approximately 1.1,<sup>7</sup> a degree of anisotropy generally not detectable by eye. This elongation may well be a consequence of convergent extension<sup>6,9</sup> and, in turn, may be a significant factor in the relatively strong preferential mitosis orientation.<sup>10</sup>

The new intensity-based algorithm presented here represents a significant improvement over previous approaches for identifying mitosis locations and orientations in pigmented epithelium. Provided that cells are imaged with at least 50 pixels per average cell diameter, the algorithm can achieve a performance of 90% and angular accuracies of 15°, more than adequate for describing mitosis frequency, spatial distribution, and orientation patterns. For decades, biomechanicians have been striving to construct a comprehensive and unified understanding of the mechanics of embryo morphogenesis, but the puzzle has been incomplete. The new pieces of data this algorithm makes possible may help to complete the puzzle.

## ACKNOWLEDGMENTS

This research was funded by the Natural Sciences and Engineering Research Council of Canada (NSERC) through Discovery Grants to GWB and DC, an NSERC Network of Centres of Excellence (NCE) GEomatics for Informed DEcisions (GEOIDE) award to DC and a CGS-M Scholarship to PS. Animals were cared for in accordance with Canadian Council on Animal Care (CCAC) guidelines.

## REFERENCES

- <sup>1</sup>Benko, R., and G. W. Brodland. Measurement of in vivo stress resultants in neurulation-stage amphibian embryos. *Ann. Biomed. Eng.* 35:672–681, 2007.
- <sup>2</sup>Bewes, J. M., N. Suchowerska, and D. R. McKenzie. Automated cell colony counting and analysis using the circular Hough image transform algorithm (CHiTA). *Phys. Med. Biol.* 53:5991–6008, 2008.
- <sup>3</sup>Bollea, A., M. Masseroli, A. Nicotra, P. Beccaglia, S. Sen, E. Erba, and G. Balconi. Automatic quantitation of cell colonies on Petri dishes by computerized image analysis. *Cytotechnology* 17:185–191, 1995.
- <sup>4</sup>Bordzilovskaya, N. P., T. A. Dettlaff, S. T. Duhon, and G. M. Malacinski. Developmental-stage series of the axolotl. In: *Developmental Biology of the Axolotl*, edited by J. B. Armstrong and G. M. Malacinski. New York: Oxford University Press, 1989.
- <sup>5</sup>Bottigli, U., M. Carpinelli, P. L. Fiori, B. Golosio, A. Marras, G. L. Masala, and P. Oliva. A new automatic system of cell colony counting. *World Acad. Sci. Eng. Tech.* 15:159–163, 2006.
- <sup>6</sup>Brodland, G. W. Do lamellipodia have the mechanical capacity to drive convergent extension? *Int. J. Dev. Biol.* 50:151–155, 2006.
- <sup>7</sup>Brodland, G. W., D. I. Chen, and J. H. Veldhuis. A cell-based constitutive model for embryonic epithelia and other planar aggregates of biological cells. *Int. J. Plast.* 22:965–995, 2006.
- <sup>8</sup>Brodland, G. W., M. J. Scott, A. F. MacLean, M. Globus, S. Vethamany-Globus, R. Gordon, J. H. Veldhuis, and R. Del Maestro. Morphogenetic movements during axolotl neural tube formation tracked by digital imaging. *Dev. Gen. Evol.* 205:311–318, 1996.
- <sup>9</sup>Brodland, G. W., and J. H. Veldhuis. Lamellipodium-driven tissue reshaping: a parametric study. *Comput. Methods Biomech. Biomed. Eng.* 9:17–23, 2006.
- <sup>10</sup>Brodland, G. W., and J. H. Veldhuis. Computer simulations of mitosis and interdependencies between mitosis orientation, cell shape and epithelia reshaping. *J. Biomech.* 35:673–681, 2002.
- <sup>11</sup>Burnside, M. B., and A. G. Jacobson. Analysis of morphogenetic movements in the neural plate of the newt *Taricha Torosa*. *Dev. Biol.* 18:537–552, 1968.
- <sup>12</sup>Chen, X., and G. W. Brodland. Mechanical determinants of epithelium thickness in early-stage embryos. *J. Mech. Behv. BioMed. Mat.* 2:494–501, 2009.
- <sup>13</sup>Davis, J., and M. Goadrich. The relationship between precision-recall and ROC curves. In: *Proceedings of the 23rd International Conference on Machine Learning*, Pittsburgh, PA, pp. 233–240, 2006.
- <sup>14</sup>Dougherty, E. R., and R. A. Lotufo. *Hands-on Morphological Image Processing*. SPIE Press, 2003.
- <sup>15</sup>Fauvel, J., R. Flood, and R. Wilson. *Möbius and his Band: Mathematics and Astronomy in Nineteenth-century, Germany*. Oxford University Press, 1993.
- <sup>16</sup>Fua, P., and Y. G. Leclerc. Object-centered surface reconstruction: combining multi-image stereo and shading. *Int. J. Comput. Vision* 16:35–56, 1995.
- <sup>17</sup>Iles, P. J. W., G. W. Brodland, D. A. Clausi, and S. M. Puddister. Estimation of cellular fabric in embryonic epithelia. *Comput. Methods Biomech. Biomed. Eng.* 10:75–84, 2007.
- <sup>18</sup>Jacobson, C. O., and A. Jacobson. Studies on morphogenetic movements during neural tube closure in amphibia. *Zoon* 1:17–21, 1973.
- <sup>19</sup>Kate, T., J. A. M. Belien, A. W. M. Smeulders, and J. P. A. Baak. Method for counting mitoses by image processing in feulgen stained breast cancer sections. *Cytometry* 14:241–250, 1993.
- <sup>20</sup>Mahadevan, S., and D. P. Casasent. Detection of triple junction parameters in microscope images. In: *Proceedings of the Photo-Optical Instrumentation Engineers (SPIE)* 2001.4387, pp. 204–214, 2001.
- <sup>21</sup>Manning, C. D., P. Raghavan, and H. Schütze. *Introduction to Information Retrieval*. Cambridge University Press, 2008.

- <sup>22</sup>Parida, L., D. Geiger, and R. Hummel. Junctions: detection, classification, and reconstruction. *IEEE Trans. Pattern Anal. Mach. Intell.* 20:687–698, 1998.
- <sup>23</sup>Phukpattaranont, P., and P. Boonyaphiphat. Color based segmentation of nuclear stained breast cancer cell images. *ECTI Trans. Elec. Eng. Electron. Comm.* 5:158–164, 2007.
- <sup>24</sup>Pilet, J., V. Lepetit, and P. Fua. Fast non-rigid surface detection, registration and realistic augmentation. *Int. J. Comput. Vision* 76:109–122, 2008.
- <sup>25</sup>Puddister, S. Estimating Bulk Geometrical Properties of Cellular Structures. Master's Thesis, University of Waterloo, 2003.
- <sup>26</sup>Sclaroff, S., and J. Isidoro. Active blobs: region-based, deformable appearance models. *Comput. Vis. Image Und.* 89:197–225, 2003.
- <sup>27</sup>Shimada, T., K. Kato, A. Kamikouchi, and K. Ito. Analysis of the distribution of the brain cells of the fruit fly by an automatic cell counting algorithm. *Physica A* 350:144–149, 2005.
- <sup>28</sup>Singh, A. Optic Flow Computation: A Unified Perspective. IEEE Press, 1990.
- <sup>29</sup>Siva, P. Quantifying the Frequency and Orientation of Mitoses in Embryonic Epithelia. Master's Thesis, University of Waterloo, 2007.
- <sup>30</sup>Siva, P., G. W. Brodland, and D. Clausi. Detection of mitoses in embryonic epithelia using motion field analysis. *Comput. Methods Biomech. Biomed. Eng.* 12:151–163, 2009.
- <sup>31</sup>Siva, P., G. W. Brodland, and D. Clausi. Automated detection of mitosis in embryonic tissues. In: Proceedings of the Fourth Canadian Conference on Computer and Robot Vision, Montreal, PQ, May 28–30, 2007, pp. 97–104, 2007.
- <sup>32</sup>Sluzek, A. A local algorithm for real-time junction detection in contour images. *Lect. Notes Comput. Sci.* 2124:465–472, 2001.
- <sup>33</sup>Talukder, A., and D. Casasent. Multiscale Gabor wavelet fusion for edge detection in microscopy images. *SPIE* 3391:336–347, 1998.
- <sup>34</sup>Tao, H., and T. S. Huang. Connected vibrations: a modal analysis approach for non-rigid motion tracking. In: IEEE Computer Society Conference on Computer Vision and Pattern Recognition (CVPR), pp. 735–740, 1998.
- <sup>35</sup>Thrun, S., W. Burgard, and D. Fox. Probabilistic Robotics. The MIT Press, 2005.
- <sup>36</sup>Veldhuis, J. H., and G. W. Brodland. A deformable block-matching algorithm for tracking epithelial cells. *Image Vis. Comp.* 17:905–911, 1999.
- <sup>37</sup>Veldhuis, J. H., G. W. Brodland, C. J. Wiebe, and G. J. Bootsma. Multiview robotic microscope reveals the in-plane kinematics of amphibian neurulation. *Ann. Biomed. Eng.* 33:821–828, 2005.
- <sup>38</sup>Vincent, L. M., and B. R. Masters. Morphological image processing and network analysis of cornea endothelial cell images. *Image Algebra Morphol. Image Process. III* 1769:212–226, 1992.